

DOI: 10.17725/rensit.2022.14.359

The Own Radiothermal Radiation of the Earth's Surface Receiving Process Modeling

Igor A. Sidorov, Alexander G. Gudkov, Sergey V. Chizhikov

Bauman Moscow State Technical University, <https://bmstu.ru/>

Moscow 105005, Russian Federation

E-mail: igorasidorov@yandex.ru, profgudkov@gmail.com, chizhikov95@mail.ru

Evgeny P. Novichikhin

Kotelnikov Institute of Radioengineering and Electronics of RAS, Fryazino Branch, <http://fire.relarn.ru/>

Fryazino 141190, Moscow Region, Russian Federation

E-mail: epnov@mail.ru

Andrey G. Bolotov, Nikolay F. Khokhlov

Russian State Agrarian University-Moscow Timiryazev Agricultural Academy, <https://www.timacad.ru/>

Moscow 127434, Russian Federation

E-mail: agbolotov@gmail.com, dok-boblov.ru@mail.ru

Igor O. Porokhov

Berg Central Scientific-Research Radioengineering Institute, <http://cnirti.ru/>

Moscow 107078, Russian Federation

E-mail: ds4@cnirti.ru

Received July 27, 2022, peer-reviewed August 03, 2022, accepted August 10, 2022

Abstract: The receiving model of the own soil radiothermal radiation by a bipolarized microwave radiometer when remote sensing the soil moisture from an unmanned aerial vehicle on low altitude is considered. The simulation is carried out taking into account the receiving antenna pattern with side lobes. The height, speed of the carrier and the main lobe axis angle are taken into account. The main parameters of the microwave radiometer for remote determination of portraits of moistened soils are given. The Earth's surface is modeled by a two-dimensional distribution function of the soil permittivity on the thickness of the near-surface layer and a deeper layer with a different permittivity value. The two-dimensional permittivity distribution function represents as "checkerboard" with a periodic change in the permittivity of the soil by "cells". Both the proper radiothermal radiation of the soil and the relict sky radiation of the celestial sphere, re-reflected by the earth's surface, are taken into account. The perspective of using the simulation results to optimize the parameters of the radiometer and remote sensing system according to the criterion of maximum sensitivity of the system to variations in soil moisture content is analyzed.

Keywords: microwave radiometer, remote sensing, soil moisture, radiation pattern, two-polarization antenna, radio brightness temperature, relict sky radiation

UDC 612.087

Acknowledgments: The study was carried out with a grant from the Russian Science Foundation No. 22-19-00063 <https://rscf.ru/project/22-19-00063>.

For citation: Igor A. Sidorov, Evgeny P. Novichikhin, Alexander G. Gudkov, Sergey V. Chizhikov, Andrey G. Bolotov, Nikolay F. Khokhlov, Igor O. Porokhov. The Own Radiothermal Radiation of the Earth's Surface Receiving Process Modeling. *RENSIT: Radioelectronics. Nanosystems. Information technologies*, 2022, 14(4):359-372e. DOI: 10.17725/rensit.2022.14.359.

CONTENTS

- 1. INTRODUCTION (360)**
 - 2. OPERATION PRINCIPLE (362)**
 - 3. ANTENNA PATTERN MODEL (364)**
 - 4. THE EARTH'S LITHOSPHERE SURFACE LAYER MODEL (365)**
 - 5. THE SURFACE RADIO THERMAL EMISSION RECEPTION MODEL (366)**
 - 6. SIMULATION RESULTS (368)**
 - 7. DISCUSSION (369)**
 - 8. CONCLUSION (369)**
- REFERENCES (370)**

1. INTRODUCTION

Precision farming has been developing intensively over the past decade in response to the growing demand for food for a growing population. Precision farming technologies ensure efficient use and management of available resources to increase crop production, reduce freshwater consumption, preserve land fertility and protect the environment. Unlike traditional agricultural technologies, precision farming uses an approach with a variable rate of application of fertilizers, water and protective equipment in the practice of growing plants [1].

Large-scale effective implementation of precision farming depends on the availability and cost of advanced tools and technologies suitable for the agricultural industry, such as intelligent machinery and robotics, global positioning system (GPS), sensor networks and monitoring, information collection and processing systems, etc. One of the key components of precision agriculture is remote sensing equipment responsible for measuring and processing data on the state (soil and agrophytocenoses). Remote monitoring in combination with satellite navigation data is used to build geographic digital maps of

field humidity and temperature to control and optimize crop cultivation modes [2-4].

In the field of remote sensing, monitoring of soil moisture is of particular interest due to global climate change in the main agricultural regions and the extremely large volume of fresh water used for irrigation. Campbell et al. [5] reported that more than 70% of the world's fresh water is used for agricultural purposes. The level of moisture content in the soil mainly determines the biophysical processes that affect crop yields and the state of soil fertility. Thus, extended and detailed information about soil moisture is a key input parameter for a precision farming system and water flow control. Further processing of geoinformation data on humidity with the help of advanced digitized agricultural management leads to a significant improvement in freshwater conservation and an increase in crop production [4].

Over the past decades, several technologies for determining soil moisture have been developed, based on various physical principles and applicable for precision farming. These technologies differ in their intended purpose, practical application, accuracy, cost, weight, etc. However, the most suitable solution for determining soil moisture for precision farming is a mobile, lightweight, high-precision measuring system that provides remote measurement of soil temperature and humidity. The demand for such a system is associated with a growing number of monitoring applications based on unmanned aerial vehicles integrated into the infrastructure of precision agriculture. Mobile sensor equipment is also suitable for integration into agricultural intelligent machinery and robotics [2], [3], [6].

Traditional methods for determining soil moisture are usually based on stationary sensors or sampling soil with analysis in the laboratory. These methods use various physical principles, such as laboratory analysis of a soil layer sample

by gamma radiation; the method of borehole neutron scattering (neutron probe); various electromagnetic sensing technologies, etc. [7]-[9] Traditional methods are actually point-based measurement methods that make the development of a soil moisture map extremely difficult if the number of measurement points is insufficient. Obviously, these methods cannot be widely used in applications where the mobility of a sensitive device is important.

For the purposes of aerial and satellite monitoring, various advanced methods have been developed to provide remote measurement of soil moisture. Technologies of remote sensing of soil moisture are widely represented by two methods: active sensing, in which the device reads reflected electromagnetic energy (radar), and passive sensing, in which the energy emitted by the earth is recorded (radiometry). Remote sensing systems deployed in the Earth observation satellite system are designed to work on a large scale or global mapping. Two projects were launched to collect data on soil moisture using satellite monitoring systems: (1) NASA Mission "Active Passive Soil Moisture" (SMAP) [10], [11] and "Soil Moisture and Ocean Salinity" (SMOS) of the European Space Agency (ESA) [12], [13]. However, the measurement accuracy provided by satellite monitoring systems is not suitable for precision farming. The best resolution of SMAP is 3 km in radar mode [11], while the spatial resolution of the SMOS system is approximately 40 km [13]. Such spatial resolution is sufficient to solve global problems of meteorology, but it is completely insufficient for the use of data in a precision farming system. Promising methods developed in recent years include various ground-based radiometric and radar systems, as well as sensing methods using electromagnetic induction. Such systems for measuring soil moisture are considered the best sensors for unmanned mobile applications of precision

farming. The most promising method is the technology of microwave radiometry. This is a passive method of microwave sensing using a highly sensitive radiometric receiver – a microwave radiometer that determines the parameters of natural thermal radiation emitted by the earth's surface. The received data of the microwave radiometer represent the radio brightness temperature of the earth's surface [14]. Further processing of the data converts them into a soil moisture value linked to a specific geographical location. The microwave radiometer technology makes it possible to develop a device for monitoring soil moisture with minimal size, weight and cost. Simultaneous use of several frequency reception bands permits to obtain data for calculating soil moisture at different depths, that is, to determine the portrait of the soil moisture profile.

The development of a new portable multi-frequency dual-polarization microwave radiometer for precision farming systems capable of operating on board an unmanned aerial vehicle is an urgent task. Microwave radiometric moisture meters are used not only for precision farming tasks, but also for solving a number of practical tasks [15], such as monitoring the hydrological situation along highways [16] and pipelines [17], as well as for searching for places of underground leaks of earthen dams and places of erosion of dams [18], detecting foci of forest fires [19] and the detection of oil films on the water surface [20]. When developing a microwave radiometer, an important aspect is to optimize the selection of parameters of the microwave radiometer and the remote sensing system as a whole, ensuring maximum sensitivity of the sensing system to variations in soil humidity and temperature. The fastest and cheapest way to optimize the selection of parameters of a microwave radiometric system is modeling.

The purpose of this article is to demonstrate the results of modeling the process of radiometric reception of own radiothermal radiation of the Earth's surface, taking into account the antenna pattern, the model of the underlying surface and the model of the sounding system, taking into account the altitude and flight speed of the carrier, as well as the angle of inclination of the axis of the main lobe of the antenna pattern.

A model is known for receiving the human body's own radiothermal radiation [21], [22] by a multi-channel, multi-frequency microwave radiothermograph used for non-invasive detection of thermal anomalies inside the human or animal body [23]-[27]. The known model cannot be used to calculate the radio brightness temperatures of the underlying surface, since it does not take into account the radiation pattern of the antenna applicator, but can be taken as a basis for modeling the earth's surface.

2. OPERATION PRINCIPLE

The principle of remote measurement of soil moisture is known [15] and is used in practice together with an unmanned aerial vehicle to build maps of soil moisture and temperature in the interests of precision farming systems. The placement of the microwave radiometer on an unmanned aerial vehicle (quadcopter) is shown in **Fig. 1** of the L-band microwave



Fig. 1. *The microwave radiometer on a quadcopter installation.*

radiometer represents the assembly of a bipolarized antenna with a receiver. The size of the microwave radiometer is determined by the size of the antenna, which is determined by the operating wavelength and the required width of the main lobe of the antenna pattern. The printed type antenna is assembled from two printed circuit boards with a size of 360x360 mm. There are four vibrators on the outer board, microstrip adders and output connectors for signals of "horizontal" and "vertical" polarization are located on the inner board. The picture of the antenna with an infrared temperature sensor is shown in **Fig. 2**. The main technical parameters of the microwave radiometer are presented in **Table 1**.

The microwave radiometer is assembled according to the well-known [15] scheme of a two-references modulation radiometer, has two internal temperature reference source with different temperatures and a microwave switch for periodic connection to the receiver input the signals from the antenna outputs and reference sources. The output signal of the receiver is converted into digital form

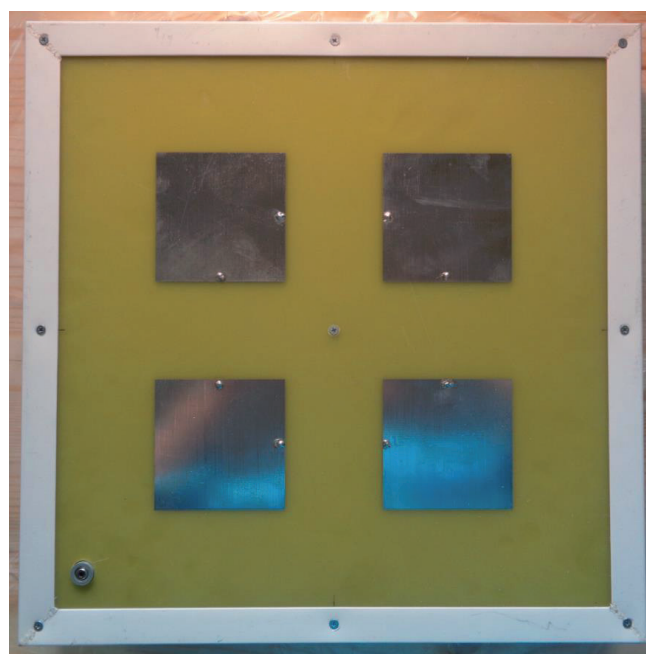


Fig. 2. *The antenna with an IR sensor picture.*

Table 1
The main technical parameters of the microwave radiometer

Parameter	Value
Central frequency, MHz	1420
Receiver band, MHz	50
The receiving channels Number	2
Vertical and horizontal polarizations	
Observation method	Along flight
Observation width, resolving element, H-flight altitude	1.0xH
Sensitivity, K	1.0
Memory type	SD-Card
Recording time, not less, Hours	3
Antenna pattern main lobe width, deg.	±30
Antenna scattering value, %	73
Supply voltage, V	12
Power consumption, Wt	5.8
Mass, kg	2.8
Size, mm	360x360x40

and transmitted to the microcontroller, which stores data on a flash card together with information from the infrared sensor located in the antenna box and navigation sensors – the receiver of the satellite navigation system, as well as from the three-axis accelerometer. The block diagram of a microwave radiometer with sensors is shown in **Fig. 3**. The microwave radiometer is placed on an unmanned aerial vehicle so that the axis of the main lobe of the antenna pattern would be directed forward along the course of the aircraft at an angle



Fig. 4. The Earth's surface sensing from a quadcopter scheme.

of 30 degrees to the vertical. The scheme of sensing the Earth's surface from a quadcopter is shown in **Fig. 4**. The quadcopter, according to a given control program, automatically flies at a given altitude along parallel lines above the test field, with data recorded on a memory card. After landing, the data card is transferred to the personal computer and the data are processed. As a result of data processing, two geo-referenced maps are created - a map of soil moisture content and a map of soil surface temperatures.

The data from an infrared temperature sensor and navigation data are used to make a temperature map. The humidity map is calculated in two stages, first the radio brightness temperatures are calculated by horizontal and vertical polarizations, then on their basis and taking into account the temperature of the soil surface, the complex dielectric permittivity of the soil is calculated, which can be converted into soil moisture and the degree of soil mineralization. It should be noted that the accuracy of the brightness-humidity recalculation of the known algorithms depends on many factors, in particular, on the type of vegetation cover, the amount of biomass, plant height, etc. The recalculation algorithms are known [15] and are not the subject of this article. In this article,



Fig. 3. The microwave radiometer with sensors block diagram.

the simplest two-layer soil model will be considered without taking into account the shielding effect of vegetation cover.

3. ANTENNA PATTERN MODEL

The antenna is the most important element of the radiometric system that determines overall dimensions, spatial resolution, noise protection and other parameters. The antenna pattern is the most important characteristic of the antenna. The radiation pattern of the real antenna (Fig. 2) of the radiometric system was measured on a special collimator and is known. However, for modeling, it is convenient to use a simulated radiation pattern so that it would be possible to track the influence of antenna radiation pattern parameters on the parameters of the radiometric system as a whole. The simplest idealized antenna with a square aperture of size D cm and with an average wavelength λ cm. was chosen as the model. The amplitude-phase distribution of the field in the antenna opening is considered uniform. The radiation pattern of the power of such an antenna is described by the function:

$$D_n(\alpha, \beta) = \left(\frac{\sin(\pi \frac{D}{\lambda} \alpha)}{\pi \frac{D}{\lambda} \alpha} \right)^2 \times \left(\frac{\sin(\pi \frac{D}{\lambda} \beta)}{\pi \frac{D}{\lambda} \beta} \right)^2, \quad (1)$$

where α and β are angular coordinates in radians, calculated from the normal to the antenna plane or the axis of the main lobe of the radiation pattern. The graph of the function of the radiation pattern in the Cartesian coordinate system for the wavelength $\lambda = 21$ cm and $D = 2\lambda$ at one of the angles is shown in Fig. 5. When modeling the antenna, only radiation from the front hemisphere was taken into account. The radiation from the rear hemisphere was considered to be zero. With these antenna parameters, the width of the main lobe of

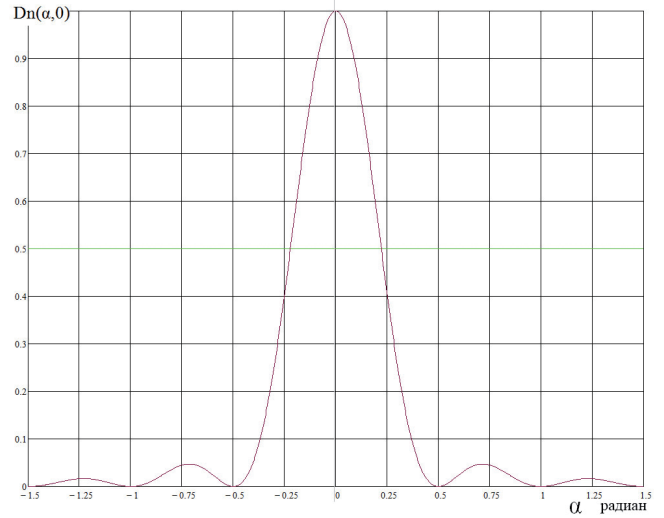


Fig. 5. Antenna radiation pattern on one of the coordinates.

the radiation pattern at the level of -3 db. is $\pm s$, where $s = 0.22$ radians. An important parameter of the antenna is the scattering coefficient γ , which is defined as:

$$\gamma = 1 - \frac{\int_{-s}^{+s} D_n(\alpha, 0) d\alpha}{\int_{-\pi}^{+\pi} D_n(\alpha, 0) d\alpha}. \quad (2)$$

The physical meaning of it is that it shows what proportion of the signal energy is received along the side lobes, in relation to the total energy along the entire directional pattern. For the considered case, the antenna

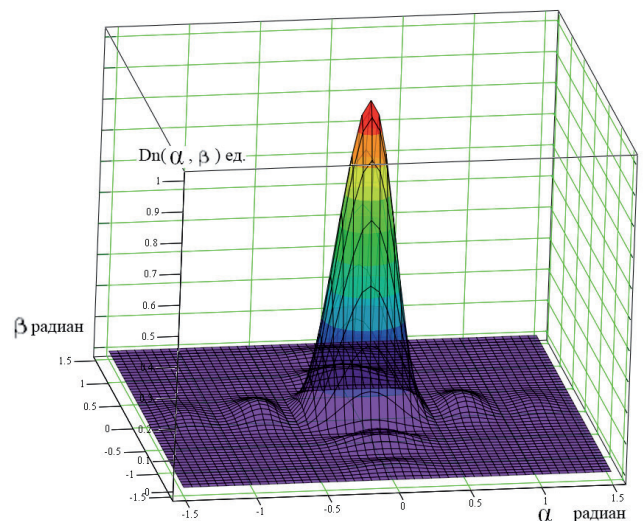


Fig. 6. Antenna radiation pattern on 3D graph.

scattering coefficient is approximately 27%. From the graph in Fig. 5, it can be seen that in the anterior hemisphere along the α coordinate, in addition to the main lobe, there are two side lobes to the right and left of the main one. The level of the first side lobe is about -13 db. The level of the second side lobe is about -18 db. The appearance of the radiation pattern in the form of a 3D graph is shown in Fig. 6.

4. THE EARTH'S LITHOSPHERE SURFACE LAYER MODEL

In physical and geological terms, the soil as an object of modeling is a complex material formed from solid-phase individual particles, as well as voids filled with aqueous solutions of salts or gaseous bubbles. Due to this, they occupy a place between the solid and the fluids. Modeling the soil's own electromagnetic radiation is an extremely difficult task, due to the wide variety of soil types, biochemical composition, vegetation cover, relief, surface roughness and hydrology. In general, the problem has not been solved so far. Therefore, simplified models are used in practice [28], taking into account only a part of the listed soil parameters.

In the proposed model, the soil is considered as a homogeneous two-layer medium with flat surfaces of sections without vegetation cover and roughness. The thickness of the near-surface layer G , the complex dielectric permittivity of the near-surface layer $\epsilon_1' + i\epsilon_1''$, where are used as soil parameters. ϵ_1' is the real part, and ϵ_1'' is the imaginary part. Similarly, the permittivity of the deep layer $\epsilon_2' + i\epsilon_2''$, is given, where ϵ_2' is the real part, and ϵ_2'' is the imaginary part (see Fig. 4).

The spatial distribution of the dielectric permittivity of the soil over the surface is impractical to consider uniform, since in this case, as a result of modeling, it would not be

possible to determine the distortions of the initial field due to the influence of the side lobes of the antenna pattern, and they, more precisely, the possibility of their correction, is of particular interest. As shown in [29], such a correction is possible if the antenna scattering coefficient does not exceed 50%.

As a model of the surface field, a periodic sequence of squares with a side of P meters of two types, arranged like the fields of a chessboard, is chosen. Such a structure is not a model of real soil, but is a convenient tool for studying the characteristic properties of the model.

The squares of the conventionally "white" type have dielectric permittivity of the soil model by layers, as described above $\epsilon_{1w} = \epsilon_1' + i\epsilon_1''$ and $\epsilon_{2w} = \epsilon_2' + i\epsilon_2''$. And conditionally, the "black" squares have additives to the dielectric permittivity of the layers so that the complex dielectric permittivity of the near-surface layer $\epsilon_{1b} = \epsilon_1' + \Delta_1' + i(\epsilon_1'' + \Delta_1'')$, respectively, the complex dielectric permittivity of the deep layer $\epsilon_{2b} = \epsilon_2' + \Delta_2' + i(\epsilon_2'' + \Delta_2'')$.

It is convenient to set a mathematically described two-dimensional function describing the terrain of the "chessboard" type using a

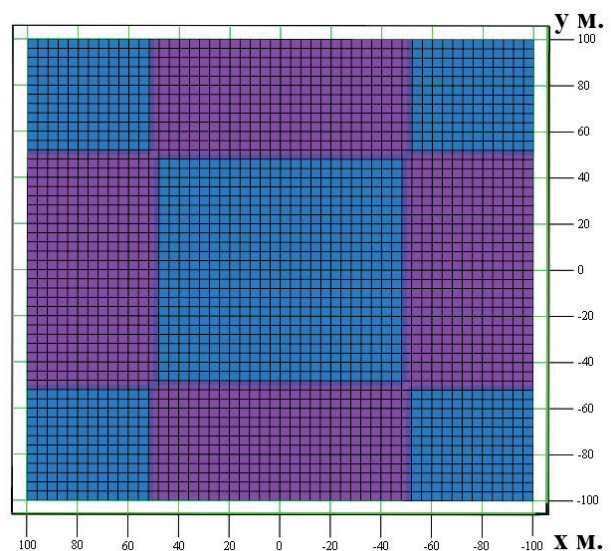


Fig. 7. The "Chessboard" function sample.

function in a rectangular Cartesian coordinate system:

$$W(x, y) = \left| \Theta(\cos(P\pi x)) + \Theta(\cos(P\pi y)) - 1 \right|, \quad (3)$$

where P is a parameter specifying the size of the "chessboard" cell, and Θ is a Heaviside function equal to zero for negative argument values and one for all others. The appearance of the function $W(x, y)$ for $P = 2$ is shown in **Fig. 7**.

Using the function $W(x, y)$, it is easy to describe the distribution of the dielectric constant of the field in x, y coordinates over the layers:

$$W_{\varepsilon_1}(x, y) = \varepsilon_1' + i\varepsilon_1'' + (\Delta_1' + i\Delta_1'') \cdot W(x, y), \quad (4)$$

$$W_{\varepsilon_2}(x, y) = \varepsilon_2' + i\varepsilon_2'' + (\Delta_2' + i\Delta_2'') \cdot W(x, y). \quad (5)$$

The functions $W_{\varepsilon_1}(x, y)$ and $W_{\varepsilon_2}(x, y)$ are used to simulate the soil's own radiation and simulate the relic radiation of the celestial sphere reflected from the earth.

5. THE SURFACE RADIO THERMAL EMISSION RECEPTION MODEL

When making field experiments, a microwave radiometer is installed on an unmanned aerial vehicle (Fig. 1), which, according to the program, flies over a given trajectory at a given height H and at a given speed V . The sensing scheme is shown in Fig. 4. The viewing angle Q_0 is calculated from the vertical and is usually selected about 30 degrees. As a result of probing the surface, the microwave radiometer measures two antenna temperatures in horizontal and vertical polarizations at each spatial position.

As a result of the simulation, two antenna temperatures should also be calculated by horizontal and vertical polarizations as a function of the parameters of the antenna pattern models, the parameters of the Earth surface model and the parameters of the surface survey system model.

$$T_{AV} = f_V(x_0, y_0, D, \lambda, G, \varepsilon_1, \varepsilon_2, \Delta_1, \Delta_2, Q_0, H, T_0, T_s), \quad (6)$$

$$T_{AH} = f_H(x_0, y_0, D, \lambda, G, \varepsilon_1, \varepsilon_2, \Delta_1, \Delta_2, Q_0, H, T_0, T_s), \quad (7)$$

where x_0, y_0 and H are the Cartesian coordinates of a quadcopter with a microwave radiometer, T_0 is the thermodynamic temperature of the soil surface, T_s is the temperature of the relic radiation of 2.33 degrees on the Kelvin scale. It is assumed that the flight speed and the axis of sight are directed along the X axis. Modeling consists in finding analytical expressions or algorithms for calculating the functions f_V and f_H and calculating antenna temperatures from vertical and horizontal polarizations. The antenna temperature for any polarization is calculated using the antenna smoothing equation [29]:

$$T_A(\alpha_0, \beta_0) = \iint T_b(\alpha, \beta) D_n(\alpha - \alpha_0, \beta - \beta_0) d\beta d\alpha, \quad (8)$$

were α_0, β_0 – coordinates of the point of sight in the polar coordinate system associated with the antenna. In formula (8), both the radiation pattern and the distribution of the brightness temperature field over the earth's surface are set in the polar coordinate system associated with the antenna. The brightness temperature map is constructed in a system of Cartesian coordinates (or geographical latitude-longitude) associated with the terrain (or north-east directions). To create a single model that takes into account both the antenna pattern model and the model of the Earth's surface and the sounding model, it is necessary to reduce all models to one common coordinate system, for example, to a Cartesian coordinate system associated with the earth.

The conversion of polar coordinates to Cartesian coordinates can be done using the formulas:

$$\alpha(x) = Q_0 - \arctg\left(\frac{x}{H}\right), \quad (9)$$

$$\beta(x, y) = \arctg\left(\frac{y \cdot \cos(Q_0)}{H}\right). \quad (10)$$

Substituting (9) and (10) into (1) we obtain the expression of the radiation pattern in Cartesian coordinates

$$D_nXY(x, y) = D_n(\alpha(x), \beta(x, y)). \quad (11)$$

The function $D_nXY(x, y)$ represents the weighting factor for the plot with the coordinates x, y of the terrain area of the size $dxdy$. The view of the function $D_nXY(x, y)$ for viewing from a height of 10 meters from a point with coordinates (0, 0, 10 m) at an angle of 30 degrees to the vertical is shown in **Fig. 8**.

From the formula (6) and (7) can be obtained from (8) taking into account (11)

$$T_{av}(x_0, y_0) = \iint T_{bv}(x, y) \cdot D_nXY(x - x_0, y - y_0) dydx, \quad (12)$$

$$T_{ah}(x_0, y_0) = \iint T_{bh}(x, y) \cdot D_nXY(x - x_0, y - y_0) dydx. \quad (13)$$

To complete the construction of the model, it remains to express the distribution functions of brightness temperatures over the vertical and horizontal polarizations $T_{BV}(x, y)$ and $T_{BH}(x, y)$ through the distribution functions of the dielectric permittivity of the field in x, y coordinates over the layers from formulas (4) and (5). The soil model

described above is considered in detail in [30], where it is called a single-layer homogeneous model. The model takes into account the reflection from the surface layer of the earth:

$$T_{bv}(x, y) = T_s \cdot R_v(W_{\epsilon 1}(x, y), H) + T_0 \cdot (1 - R_v(W_{\epsilon 1}(x, y), H)), \quad (14)$$

$$T_{bh}(x, y) = T_s \cdot R_h(W_{\epsilon 1}(x, y), H) + T_0 \cdot (1 - R_h(W_{\epsilon 1}(x, y), H)), \quad (15)$$

were R_v and R_h – Fresnel reflection coefficients for vertical and horizontal polarizations, Q is the angle relative to the vertical under which the surface point with coordinates $(x, y, 0)$ is visible from the antenna location point (point with coordinates (0, 0, H)):

$$R_v(x, y) = \frac{W_{\epsilon 1}(x, y) \cdot \cos(Q) - \sqrt{W_{\epsilon 1}(x, y) - \sin^2(Q)}}{W_{\epsilon 1}(x, y) \cdot \cos(Q) + \sqrt{W_{\epsilon 1}(x, y) - \sin^2(Q)}}, \quad (16)$$

$$R_h(x, y) = \frac{\cos(Q) - \sqrt{W_{\epsilon 1}(x, y) - \sin^2(Q)}}{\cos(Q) + \sqrt{W_{\epsilon 1}(x, y) - \sin^2(Q)}}. \quad (17)$$

The angle of sight Q of a point with coordinates $(x, y, 0)$ depends on the coordinates x, y and the height of the antenna location H can be calculated by the formula (18)

$$Q = \arctg\left(\frac{\sqrt{x^2 + y^2}}{H}\right). \quad (18)$$

The cosine and the square of the sine of the angle Q can also be represented in terms of the coordinates x, y and height H :

$$\cos(Q) = \frac{H}{\sqrt{H^2 + x^2 + y^2}}, \quad (19)$$

$$\sin^2(Q) = \frac{x^2 + y^2}{(H^2 + x^2 + y^2)}. \quad (20)$$

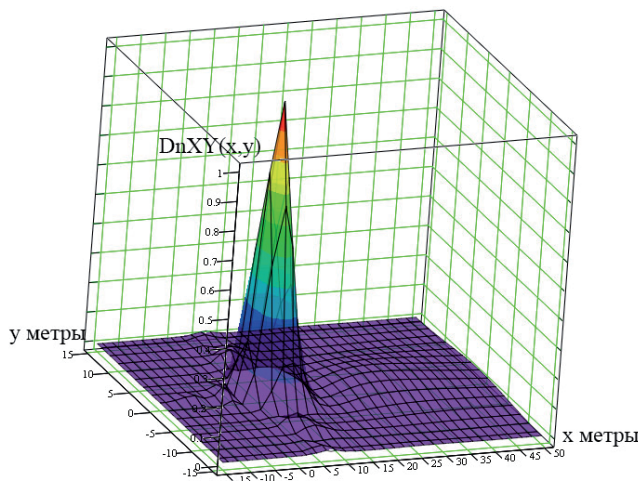


Fig. 8. Weight function $D_nXY(x, y)$ Sample.

The partially incident electromagnetic wave of the relic radiation is refracted, passes through the near-surface layer, is partially absorbed, is reflected from the interface of the near-surface and deep layer, is partially absorbed again, is partially reflected from the soil surface and is partially radiated into the open space again. The attenuation coefficient of the electromagnetic wave in the near-surface layer, according to [30]:

$$\delta(G, \lambda) = \exp\left(-4\pi\epsilon_1'' \frac{G}{\lambda \cos(Q_r)}\right), \quad (21)$$

where Q – incidence angle, G – layer thickness.

The reflection coefficients from the section of the near-surface and deep layer are given in [31] and in the accepted designations can be represented as:

$$R_{V2}(x, y, Q_r) = \frac{|W_{\epsilon_2}(x, y) \cdot \cos(Q_r) - \sqrt{W_{\epsilon_1}(x, y)} F(x, y, Q_r)|^2}{|W_{\epsilon_2}(x, y) \cdot \cos(Q_r) + \sqrt{W_{\epsilon_1}(x, y)} F(x, y, Q_r)|^2}, \quad (22)$$

$$R_{H2}(x, y, Q_r) = \frac{|W_{\epsilon_1}(x, y) \cdot \cos(Q_r) - F(x, y, Q_r)|^2}{|W_{\epsilon_1}(x, y) \cdot \cos(Q_r) + F(x, y, Q_r)|^2}, \quad (23)$$

where

$$F(x, y, Q_r) = \sqrt{W_{\epsilon_2}(x, y) - W_{\epsilon_1}(x, y) \cdot \sin^2(Q_r)}.$$

The refraction angle Q_r is related to the angle of incidence Q by the Snellius law expressed by the well-known formula (24):

$$\frac{\sin(Q_r)}{\sin(Q)} = \frac{\sqrt{W_{\epsilon_1}(x, y)}}{\sqrt{W_{\epsilon_2}(x, y)}}. \quad (24)$$

The formulas given completely define the functions (6) and (7) and are sufficient to construct a model for receiving radiothermal radiation from the soil surface.

The calculations results of using the above model are representing below.

6. SIMULATION RESULTS

The presented model can be used to calculate antenna temperatures at the output of the radiometer by vertical and horizontal polarizations depending on the parameters of the antenna, sensing and soil. As a result of calculations of integral expressions in formulas (12) and (13), two-dimensional graphs of weight functions were obtained, shown in **Fig. 9**. The functions are calculated for a uniform temperature field of 300° K, when viewed from a height of $H = 10$ m. from the origin at an angle of 30° in the direction of the X axis.

The cross sections of the surfaces represented by the plane $Y = 0$, in the range from 0 to 10 meters, are shown in **Fig. 10**. Analysis of the graphs presented in Fig. 10 shows that the coordinates of the maxima of the weight functions in vertical and horizontal polarizations do not coincide, but differ by about half a meter and do not coincide with the coordinate of the point of sight. The analysis showed that the differences arose due to differences in the properties of the Fresnel coefficients for vertical and horizontal polarizations.

The presented model allows simulating the flight of a carrier with a radiometer and calculating antenna temperatures by vertical and horizontal polarizations. An example of

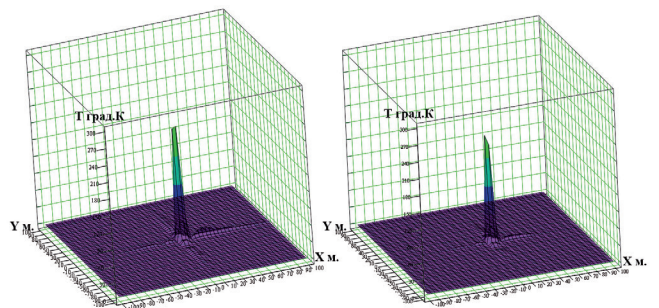


Fig. 9. Weight functions $T_v(x,y) \cdot D_nXY(x,y)$ and $T_h(x,y) \cdot D_nXY(x,y)$.

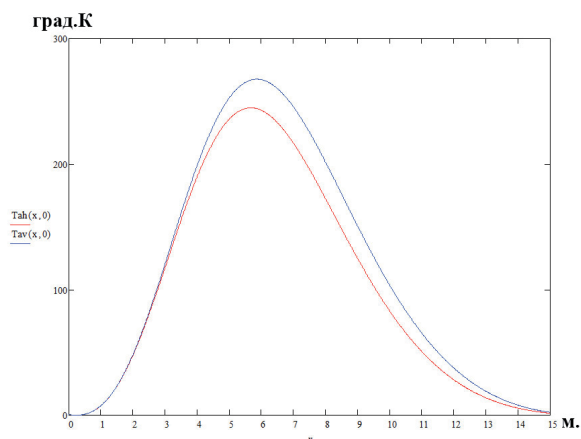


Fig. 10. The cross section of the functions $Tv(x,y) \cdot DnXY(x,y)$ and $Tb(x,y) \cdot DnXY(x,y)$ by plane $Y = 0$.

calculating antenna temperatures when the carrier moves along the X axis is shown in **Fig. 11**. The dotted line on the graph shows the boundaries of the "chessboard" cell.

The characteristic advance of the temperature graphs in comparison with the cell boundary is associated with the inclination of the axis of the radiation pattern in the direction of the flight line.

A small oscillatory process on the antenna temperature charts is due to the presence of side lobes of the antenna.

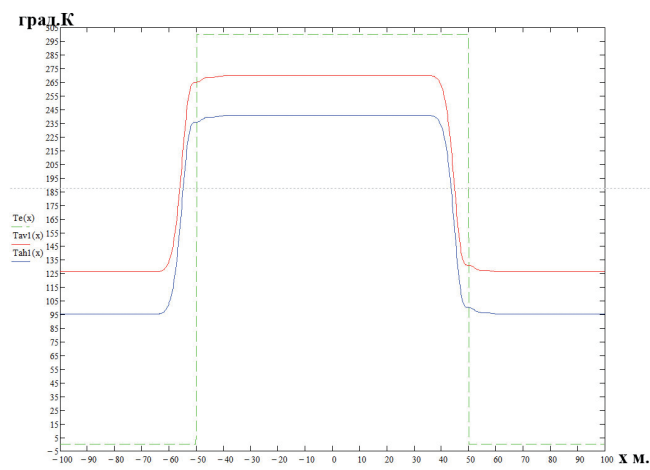


Fig. 11. Graph of calculated temperatures when the carrier moves along the X axis.

7. DISCUSSION

The presented model was calculated using a specialized mathematical program and a program written in the Delphi language. The coincidence of the calculation results confirms the adequacy of the constructed model. To calculate the graph (Fig. 11) with a mathematical program on a laptop with a quad-core processor, it took more than one hour. The same result was obtained in the Delphi program in less than one second.

The resulting model is planned to be developed, improved and used to develop a modern algorithm for correcting amplitude distortions caused by the presence of side lobes of the antenna instead of the known one [29], as well as to optimize the parameters of the radiometer and the survey system according to the criterion of maximum sensitivity to variations in soil moisture by layers.

8. CONCLUSION

As a result of the research and modeling within the framework of the represented model, the following new results were obtained:

- a model of the brightness temperature formation of the underlying surface is obtained, regarding the parameters of the antenna, radiometer, Earth's surface and the sensing system;
- the antenna temperatures on vertical and horizontal polarizations were calculated using the model, when simulating the flight of the carrier;
- the mismatch of the coordinates of the maxima of weight functions for vertical and horizontal polarizations as a result of the analysis of graphs, was found;
- the graphs for calculating antenna temperatures at the front and the decline of

the spatial pulse show a transition process due to the presence of side lobes of the antenna pattern;

REFERENCES

1. Shafi U, Mumtaz R, Garcia-Nieto J, Hassan SA, Zaidi SAR, Iqbal N. Precision agriculture techniques and practices: From considerations to applications. *Sensors*, 2019, 19(17):3796, doi: 10.3390/s19173796.
2. Tsouros DC, Bibi S, Sarigiannidis PG. A review on UAV-based applications for precision agriculture. *Information*, 2019, 10(11):349, doi: 10.3390/info10110349.
3. Maes WH, Steppe K. Perspectives for remote sensing with unmanned aerial vehicles in precision agriculture. *Trends in Plant Science*, 2019, 24(2):152-164, doi: 10.1016/j.tplants.2018.11.007.
4. Kashyap B, Kumar R. Sensing methodologies in agriculture for soil moisture and nutrient monitoring. *IEEE Access*, 2021, 9:14095-14121, doi: 10.1109/ACCESS.2021.3052478.
5. Bruce M. Campbell, Douglas J. Beare, Elena M. Bennett, Jason Hall-Spencer, John S. I. Ingram, Fernando Jaramillo, Rodomiro Ortiz, Navin Ramankutty, Jeffrey A. Sayer, Drew Shindell. Agriculture production as a major driver of the earth system exceeding planetary boundaries. *Ecology and Society*, 2017, 22(4):1-11, doi: 10.5751/ES-09595-220408.
6. Inoue Y. Satellite- and drone-based remote sensing of crops and soils for smart farming – a review. *Soil Science and Plant Nutrition*, 2020, 66(6):798-810, doi: 10.1080/00380768.2020.1738899.
7. Kodikara J, Rajeev P, Chan D, Gallage C. Soil moisture monitoring at the field scale using neutron probe. *Canadian Geotechnical Journal*, 2014, 51(3):332-345, doi: 10.1139/cgj-2012-0113.
8. Balaghi S, Ghal-Eh N, Mohammadi A, Vega-Carrillo HR. A neutron scattering soil moisture measurement system with a linear response. *Applied Radiation and Isotopes*, 2018, 142:167-172, doi: 10.1016/j.apradiso.2018.10.002.
9. Babaeian E, Sadeghi M, Jones SB, Montzka C, Vereecken H, Tuller M. Ground, proximal, and satellite remote sensing of soil moisture. *Reviews of Geophysics*, 2019, 57:530-616, doi: 10.1029/2018RG000618.
10. Entekhabi D, Njoku EG, O'Neill PE, Kellogg KH, Crow WT, Edelstein WN, Entin JK, Goodman SD, Jackson TJ, Johnson J, Kimball J, Piepmeier JR, Koster RD, Martin N, McDonald KC, Moghaddam M, Moran S, Reichle R, Shi JC, Spencer MW, Thurman SW, Tsang L, Van Zyl J. The Soil Moisture Active Passive (SMAP) mission. *Proc. of the IEEE*, 2010, 98(5):704-716, doi: 10.1109/JPROC.2010.2043918.
11. Steven K. Chan, Rajat Bindlish, Peggy E. O'Neill, Eni Njoku, Tom Jackson, Andreas Colliander, Fan Chen, Mariko Burgin, Scott Dunbar, Jeffrey Piepmeier, Simon Yueh, Dara Entekhabi, Michael H. Cosh, Todd Caldwell, Jeffrey Walker, Xiaoling Wu, Aaron Berg, Tracy Rowlandson, Anna Pacheco, Heather McNairn, Marc Thibeault, José Martínez-Fernández, Ángel González-Zamora, Mark Seyfried, David Bosch, Patrick Starks, David Goodrich, John Prueger, Michael Palecki, Eric E. Small, Marek Zreda, Jean-Christophe Calvet, Wade T. Crow, and Yann Kerr. Assessment of the SMAP passive soil moisture product. *IEEE Trans. on Geoscience and Remote Sensing*, 2016, 54(8):4994-5007, doi: 10.1109/TGRS.2016.2561938.

12. Kerr YH, Waldteufel P, Wigneron J-P, Martinuzzi J-M, Font J, Berger M. Soil moisture retrieval from space: The soil moisture and ocean salinity (SMOS) mission. *IEEE Trans. on Geoscience and Remote Sensing*, 2001, 39(8):1729-1735, doi: 10.1109/36.942551.
13. Mecklenburg Susanne, Matthias Drusch, Yann H. Kerr, Jordi Font, Manuel Martin-Neira, Steven Delwart, Guillermo Buenadicha, Nicolas Reul, Elena Daganzo-Eusebio, Roger Oliva, Raffaele Crapolicchio. ESA's soil moisture and ocean salinity mission: mission performance and operations. *IEEE Trans. on Geoscience and Remote Sensing*, 2012, 50(5):1354-1366, doi: 10.1109/TGRS.2012.2187666.
14. Ulaby FT, Long DG. *Microwave Radar and Radiometric Remote Sensing*. Ann Arbor, The University of Michigan Press, 2014.
15. Verba VS, Gulyaev Yu V, Shutko AM, Krapivin VF (eds.). *Microwave Radiometry of Land and Water Surfaces: From Theory to Practice*. Sofia, Marin Drinov Academic Publishing, 2014.
16. Sidorov IA, Soldatenko AP, Gudkov AG, Leushin VY, Novichikhin EP. Results of field experiments on monitoring the hydrological situation along highways with a multifrequency polarimetric system of microwave radiometers. *Mashinostroitel*, 2015, 12:46-55.
17. Sidorov IA, Gudkov AG, Sister VG, Ivannikova EM, Leushin VY. Monitoring of the hydrological situation along pipeline routes by means of microwave radiometry methods. *Chemical and Petroleum Engineering*, 2021, 56:929-234, doi: 10.1007/s10556-021-00864-6.
18. de Jeu R, Parinussa R, Biemond L, Haarbrink R, Shutko A, Demontoux F, Provoost Y. Safety inspection of levees with L-band radiometry. *Proc. 11th Specialist Meeting on Microwave Radiometry and Remote Sensing of the Environment*, USA, Washington, DC, 1-4 March 2010, pp. 96-98, doi: 10.1109/MICRORAD.2010.5559583.
19. Sister VG, Ivannikova EM, Gudkov AG, Leushin VY, Sidorov IA, Plyushchev VA, Soldatenko AP. Detection of forest and peat-bog fire centers by means of microwave radiometer sounding. *Chemical and Petroleum Engineering*, 2016, 52:123-125, doi: 10.1007/s10556-016-0160-2.
20. Gudkov AG, Sister VG, Ivannikova EM, Leushin VY, Plyushchev VA, Sidorov IA, Chetyrkin DY. On the possibility of detecting oil films on water surface by microwave radiometry methods. *Chemical and Petroleum Engineering*, 2019, 55:57-62, doi: 10.1007/s10556-019-00580-2.
21. Evgeny P. Novichikhin, Igor A. Sidorov, Vitaly Y. Leushin, Svetlana V. Agasieva and Sergey Chizhikov. The local heat source detection inside of the human body by means of microwave radiothermography. *RENSIT: Radioelectronics. Nanosystems. Information technologies*, 2020, 12(2):305-312, doi: 10.17725/rensit.2020.12.305.
22. Evgeny P. Novichikhin, Igor A. Sidorov, Vitaly Yu. Leushin, Svetlana V. Agasieva, Sergey V. Chizhikov. Local heat source detection inside of the human body by means of microwave radiothermography. *RENSIT: Radioelectronics. Nanosystems. Information technologies*, 2022, 14(1):103-110, doi: 10.17725/rensit.2022.14.103.
23. Sidorov IA, Gudkov AG, Leushin VY, Gorlacheva EN, Novichikhin EP, Agasieva SV. Measurement and 3D Visualization of the Human Internal Heat Field by Means of Microwave

- Radiometry. *Sensors*, 2021, 21:4005, doi: 10.3390/s21124005.
24. Vesnin S, Turnbull AK, Dixon JM, Goryanin I. Modern Microwave Thermometry for Breast Cancer. *J. Mol. Imaging Dyn.*, 2017, 7(10):1109.
25. Gudkov AG, Leushin VY, Sidorov IA, Vesnin SG, Porokhov IO, Sedankin MK, Agasieva SV, Chizhikov SV, Gorlacheva EN, Lazarenko M. et al. Use of Multichannel Microwave Radiometry for Functional Diagnostics of the Brain. *Biomed. Eng.*, 2019, 53:108-111.
26. Leushin VYu, Gudkov AG, Porokhov IO, Vesnin SG, Sedankin MK, Solov'ev YuV, Agasieva SV, Chizhikov SV. Possibilities of increasing the interference immunity of radiothermograph applicator antennas for brain diagnostics. *Sensors and Actuators A: Physical*, 2022, 337:113439, doi: 10.1016/j.sna.2022.113439.
27. Vesnin SG, Sedankin MK, Ovchinnikov LM, Gudkov AG, Leushin VY, Sidorov IA, Goryanin II. Portable microwave radiometer for wearable devices. *Sensors and Actuators A: Physical*, 2021, 318:112506, doi: 10.1016/j.sna.2020.112506.
28. Maheshwari Neelam, Andreas Colliander, Binayak P. Mohanty, Michael H. Cosh, Sidharth Misra, Thomas J. Jackson. Multiscale Surface Roughness for Improved Soil Moisture Estimation. *IEEE Transactions on Geoscience and Remote Sensing*, 2020, 58(8):5264-5276, doi: 10.1109/TGRS.2019.2961008.
29. Egorov ST, Plushev VA, Vlasov AA. Method of correction of radio brightness distribution distortions caused by the side lobes of the antenna radiation pattern, *Radioengineering and electronics*, 1981, 8:1-7.
30. Finkelstein MI, Mendelson VL, Kutev VA. *Radar of layered earth covers*. Moscow, Sovetskoe radio Publ., 1977, 176 pp.
31. Grudinskaya GP. *Propagation of radio waves*. Moscow, Vysshaya shkola Publ., 1975, 155 pp.